RSC Advances

PAPER

View Article Online
View Journal | View Issue

Cite this: *RSC Adv.*, 2025, **15**, 46737

Engineering a light-active CoO/D-CN catalyst for dual-functional enhanced BPA degradation and hydrogen evolution

Sudhansu Sekhar Behera,[a] Alaka Samal,*[b] Arundhati Barik[a] and Nigamananda Das *[b]

Received 1st August 2025
Accepted 11th November 2025

DOI: 10.1039/d5ra05595d

rsc.li/rsc-advances

Owing to the current energy and environmental crisis, the design of efficient catalysts is a critical necessity. A visible-light-responsive cobalt monoxide-based heterojunction was engineered to achieve efficient bisphenol A (BPA) degradation and hydrogen (H_2) evolution. For the formation of the heterojunction, structurally defective graphitic carbon nitride (g-C_3N_4) (abbreviated as D-CN) was designed by adding ascorbic acid during the synthesis of the g-C_3N_4. The close interface between the CoO and D-CN prevents fast charge recombination, as confirmed by the enhanced photocatalytic response and reduced photoluminescence intensity. XRD, XPS, BET surface area, TEM/SEM and EDX analyses reveal a uniform CoO composition on the D-CN matrix. In comparison to the individual components, the optimized composite shows an approximately three-fold increase in H_2 generation under visible-light illumination and a significantly better photocatalytic BPA degradation rate. This work demonstrates a synergistic approach that uses a straightforward, non-hazardous photocatalyst design to combine environmental restoration with solar fuel generation.

Introduction

In recent decades, there has been a growing trend for the fabrication of visible-light-active catalysts to tackle energy and sustainability issues.[1–4] Even at minimal levels, bisphenol A (BPA)—an endocrine disruptor commonly employed in the production of plastics—is one of the many organic pollutants that poses serious threats to the health of humans and aquatic ecosystems.[5,6] Concurrently, photocatalytic hydrogen (H_2) generation through water splitting has generated interest due to a worldwide demand for environmentally friendly renewable energy. It is still difficult but very desirable to design a simple, non-toxic catalyst that can both break down BPA and produce H_2 when exposed to visible light.

As graphitic carbon nitride is a metal-free polymeric material with a sufficient band gap (~2.7 eV), strong thermal resistance, and visible-light activity, it has been explored substantially in the field of photocatalytic applications. Despite its high redox potential and adequate band positions, the quick electron–hole recombination of graphitic carbon nitride limits its photocatalytic potential. Creating defects in the polymeric structure of graphitic carbon nitride provides more trap sites to prevent the fast recombination of photogenerated electrons and holes. Consequently, this approach can result in longer charge carrier lifetimes and improved charge mobility with a narrow band gap and modified electronic structure. Along with the electronic tuning of the catalysts, heterojunction design has become an essential strategy for minimizing the recombination of the charge carriers. Using the right combination of catalysts has become a potential approach to overcome these limitations and create a suitable heterojunction architecture, thereby broadening the light-absorption range and improving charge separation in the material. Strong visible-light absorption and a high redox potential are provided by cobalt(II) oxide (CoO), a p-type semiconductor with a narrow band gap (~2.2 eV).[7,8] Accordingly, combining CoO and D-CN into a heterojunction can lead to fascinating synergies, especially for photocatalytic applications. The interesting synergy of the CoO/D-CN heterojunction enables easy spatial separation of photogenerated charge carriers and allows them to participate in targeted redox reactions. Moreover, cobalt-based materials are earth-abundant and cost-effective, making them attractive alternatives to noble-metal cocatalysts. Various works have been conducted to explore polymer-based metal oxide heterojunctions, as shown in Table 1.

Herein, structurally defective carbon nitride was composited with cobalt monoxide to create a CoO/D-CN heterojunction, in which both materials exhibit high activity under visible light and possess suitable band gaps for efficient proton reduction and organic-contaminant degradation. In this work, we report

---

[a] *Department of Plastic Engineering, Central Institute of Petrochemicals Eng. & Tech. (CIPET), Institute of Petrochemicals Technology (IPT), Patia, Bhubaneswar, 751024, India*

[b] *Centre of Excellence in Advanced Materials and Applications (CAMA), Department of Chemistry, Utkal University, Vani Vihar, Bhubaneswar, Odisha 751004, India. E-mail: dasn.chem@utkaluniversity.ac.in; samal.alaka@utkaluniversity.ac.in*

Table 1 Comparative table of the photoactivity of polymer-based metal oxide heterojunctions

Photocatalyst system	Charge-transfer type	Photocatalytic test	Key activity	Reference
TiO_2/g-C_3N_4	Type-II	RhB/MB degradation under visible-light irradiation	Moderate photoactivity, limited by weak CB potential of TiO_2	9
ZnO/g-C_3N_4	S-Scheme/type-II	H_2 evolution and dye degradation	Enhanced *vs.* pure g-C_3N_4, moderate stability	10
CoO/g-C_3N_4	p–n type-II heterojunction	Visible-light H_2 evolution	Activity ≈ 2–3 × g-C_3N_4	11
g-C_3N_4/CoO/CoP	Hybrid type-II	Photocatalytic H_2 generation	1277.9 $\mu mol\ g^{-1}\ h^{-1}$ (≈4 × g-C_3N_4/CoO)	12
S-Doped g-C_3N_4/TiO_2	S-Scheme/type-II	Theoretical (DFT/TD-DFT) optical and electronic analysis	Improved band alignment and high charge separation	13
CoO/D-CN	Direct Z-scheme heterojunction	Visible-light BPA degradation and H_2 evolution	Retains strong redox ability, ~100% BPA degradation, ~7400 $\mu mol\ g^{-1}\ h^{-1}$ H_2	This work

the rational synthesis of a CoO/D-CN heterojunction photocatalyst *via* a facile hydrothermal strategy. The engineered heterostructure exhibits synergistically enhanced performance for both BPA degradation and H_2 generation under visible light irradiation. Morphological and compositional characterization confirms the successful formation of the composite, while photoluminescence measurements reveal improved charge transfer dynamics. Surface area analysis confirms that both D-CN and the CoO/D-CN heterostructure exhibit enhanced surface areas, demonstrating the successful introduction of defects into the polymeric structure. Compared with previously reported g-C_3N_4-based metal oxide photocatalysts,[9–13] the present CoO/D-CN system achieves a true direct Z-scheme mechanism for BPA abatement and H_2 production that has not yet been experimentally reported. The photocatalyst reported here integrates optimized band alignment, visible-light absorption, and verified radical-driven charge dynamics, leading to superior photocatalytic activity for both BPA degradation and H_2 production. The broad applicability of the photocatalyst in energy and environmental fields establishes this composite as a new benchmark for next-generation photocatalytic materials. This dual-functional system demonstrates the potential of heterojunction-based photocatalysts for integrated environmental remediation and solar energy conversion.

Materials and methods

Chemicals and reagents

All chemicals were of analytical grade and used without further purification. Cobalt nitrate hexahydrate ($Co(NO_3)_2\cdot 6H_2O$), sodium hydroxide (NaOH), urea, L-ascorbic acid and BPA were obtained from standard laboratory suppliers. Distilled water was used for all the preparation and washing steps. All syntheses were carried out using hydrothermal and thermal techniques to obtain crystalline and well-integrated nanocomposites.

Synthesis of cobalt oxide (CoO)

CoO nanoparticles were synthesized using a hydrothermal precipitation technique. In a clean beaker, a stoichiometric amount of $[Co(NO_3)_2\cdot 6H_2O]$ (0.3 M) was dissolved in 40 mL of distilled water. Separately, 1 g of NaOH was dissolved in 40 mL of distilled water. The cobalt nitrate solution was stirred magnetically, and the NaOH solution was added slowly in a dropwise manner over 30 min. The resulting mixture was transferred to a Teflon-lined autoclave and heated at 180 °C for 12 h. After natural cooling, the suspension was centrifuged and washed several times with water and ethanol until a neutral pH was achieved. The final product was dried in an oven at 80 °C for 12 h and ground into powder.

Synthesis of D-CN

To synthesize pristine g-C_3N_4, 5 g of urea was placed in a covered alumina crucible and heated at 500 °C for 2 h in a muffle furnace. During this thermal polymerization process, urea gradually decomposes and condenses into g-C_3N_4. After natural cooling to room temperature, the obtained yellow powder was collected, ground thoroughly using an agate mortar and pestle, and stored.

For the preparation of the structurally defective carbon nitride (D-CN), 0.5 wt% of L-ascorbic acid (with respect to the mass of urea) was homogeneously mixed with the precursor urea before calcination. The mixture was then transferred to a crucible and heated at 500 °C for 2 h under identical conditions. The addition of L-ascorbic acid, a mild reducing agent, facilitates the formation of nitrogen vacancies and surface defects during the thermal condensation process.

Preparation of CoO/D-CN composites

The CoO/D-CN composite was synthesized *via* a one-pot hydrothermal method. For a 1 : 1 weight ratio of D-CN to CoO (as per the target composition), a calculated amount of D-CN was first dispersed in distilled water and ultrasonicated for 45 min to form a uniform suspension. Then, an aqueous solution of cobalt nitrate $[Co(NO_3)_2\cdot 6H_2O]$ was added under continuous stirring, followed by the slow addition of the NaOH solution mentioned above.

The resulting homogeneous mixture was transferred to a Teflon-lined stainless-steel autoclave and subjected to hydrothermal treatment at 180 °C for 12 h. After naturally cooling to room temperature, the obtained solid product was collected by centrifugation, washed several times with distilled water and ethanol to remove impurities, and dried at 80 °C overnight. Finally, the dried material was lightly ground to obtain a fine CoO/D-CN heterostructure powder.

Characterization

X-ray diffraction (XRD) patterns of the metal oxide and its composite were recorded using an Empyrean XRD Instrument operated at 30 kV and 15 mA, employing Cu Kα radiation ($\lambda = 1.5406$ Å) over a 2θ range of 5–90°. The band gap energy values were calculated from UV-visible DRS recorded using a $BaSO_4$ reference on a Shimadzu UV-2400 instrument. The photoluminescence (PL) spectra were scanned on an RF-6000 spectrofluorometer. Scanning electron microscopy (Zeiss EVO) and transmission electron microscopy (TEM, JEOL JEM-F200), along with the selected area electron diffraction pattern (SAED), were used for the morphological investigations. X-ray photoelectron spectroscopy (XPS, Physical Electronics) was used to determine the oxidation states of the elements of the heterojunction. The BET surface area was determined using a Smart Sorb 92/93 surface area analyser.

Dual-functional photocatalysis over CoO/D-CN

Bisphenol A (BPA) degradation

The photocatalytic activity of the synthesized CoO/D-CN heterostructure was evaluated through the degradation of BPA under visible light irradiation. Aqueous BPA solutions were prepared at a concentration of 20 ppm using distilled water. The catalyst dosage was fixed at 0.1 g per 150 mL of BPA solution for each trial. The reaction mixture was transferred to a borosilicate glass photoreactor equipped with a magnetic stirrer. Before light exposure, the suspension was stirred in the dark for 30 min to ensure adsorption–desorption equilibrium between the BPA molecules and the catalyst surface. A 125 W halogen lamp served as the visible light source, positioned approximately 15 cm above the surface of the reactor. The system was kept close to room temperature throughout the reaction using a cooling water circulation setup. At fixed time intervals (0, 30, 60, 90, and 120 minutes), 5 mL aliquots were withdrawn and immediately centrifuged at 6000 rpm for 10 min to remove the suspended photocatalyst particles. The clear supernatant was then analyzed using a UV-visible spectrophotometer, and the absorbance was recorded at 276 nm, the characteristic absorption wavelength of BPA. The degradation efficiency was calculated using the following formula:

$$\text{Degradation\%} = ((C_0 - C_t)/C_0) \times 100$$

where C_0 is the initial absorbance of BPA C_t is the absorbance at time t.

Hydrogen evolution reaction (HER)

Photocatalytic hydrogen evolution *via* water splitting was performed in a Pyrex reactor flask under vertical illumination using a 125 W halogen lamp. For the reaction, 0.1 g of the CoO/D-CN composites was dispersed in 50 mL of an aqueous methanol solution (5 vol%), which serves as the sacrificial agent. Before visible-light exposure, the suspension was purged with nitrogen gas to remove dissolved oxygen. The evolved hydrogen (H_2) was analyzed using a gas chromatograph (GC) with reference to standard H_2 (purity: 99.99%).

Results and discussion

Morphological and elemental analysis

The morphological features of the synthesized samples were examined using scanning electron microscopy (SEM). In our previous studies,[14,15] pristine g-C_3N_4 displayed a typical sheet-like, stacked lamellar morphology and a low surface area, which is characteristic of layered graphitic materials. After defect engineering using L-ascorbic acid, the D-CN sample displayed a relatively rough and porous surface with partially exfoliated sheets, indicating the successful introduction of defects and an improved surface area and textural properties. In contrast, the CoO/D-CN composite revealed the presence of uniformly distributed CoO nanoparticles anchored on the D-CN surface. The CoO nanoparticles appeared as small, well-dispersed granules closely attached to the D-CN sheets, confirming the effective interfacial coupling between the two components. This morphology is favorable for enhancing the number of exposed active sites and facilitating charge carrier separation across the heterojunction. As can be seen in Fig. 1(a), the SEM image of pure D-CN displays a layered, sheet-like structure with a porous morphology, characteristic of a defect-containing graphitic polymer network, which provides a high surface area and abundant reactive sites. In Fig. 1(b), the SEM image of the pristine CoO nanoparticles shows aggregated, quasi-spherical particles with high surface roughness, potentially beneficial for photocatalytic activity owing to increased active sites. However, in Fig. 1(c and d), the SEM analysis of CoO/D-CN reveals the successful deposition of the CoO nanoparticles onto the structurally defective g-C_3N_4 sheets, leading to a denser and more textured structure, which enhances interfacial contact and light absorption. The energy-dispersive X-ray spectroscopy (EDX) analysis further confirmed the presence of C, N, O, and Co elements in the CoO/D-CN composite, with no detectable impurities, suggesting the high purity of the synthesized material. In Fig. 1(e), the EDX spectrum of the CoO/D-CN composite also confirms the successful incorporation of CoO into the D-CN matrix. Moreover, the elemental mapping images in Fig. 1(f) clearly demonstrate the uniform spatial distribution of all the constituent elements throughout the composite matrix, verifying the homogeneous incorporation of CoO nanoparticles onto the D-CN framework. This uniform dispersion is crucial for achieving efficient interfacial contact and improved catalytic performance.

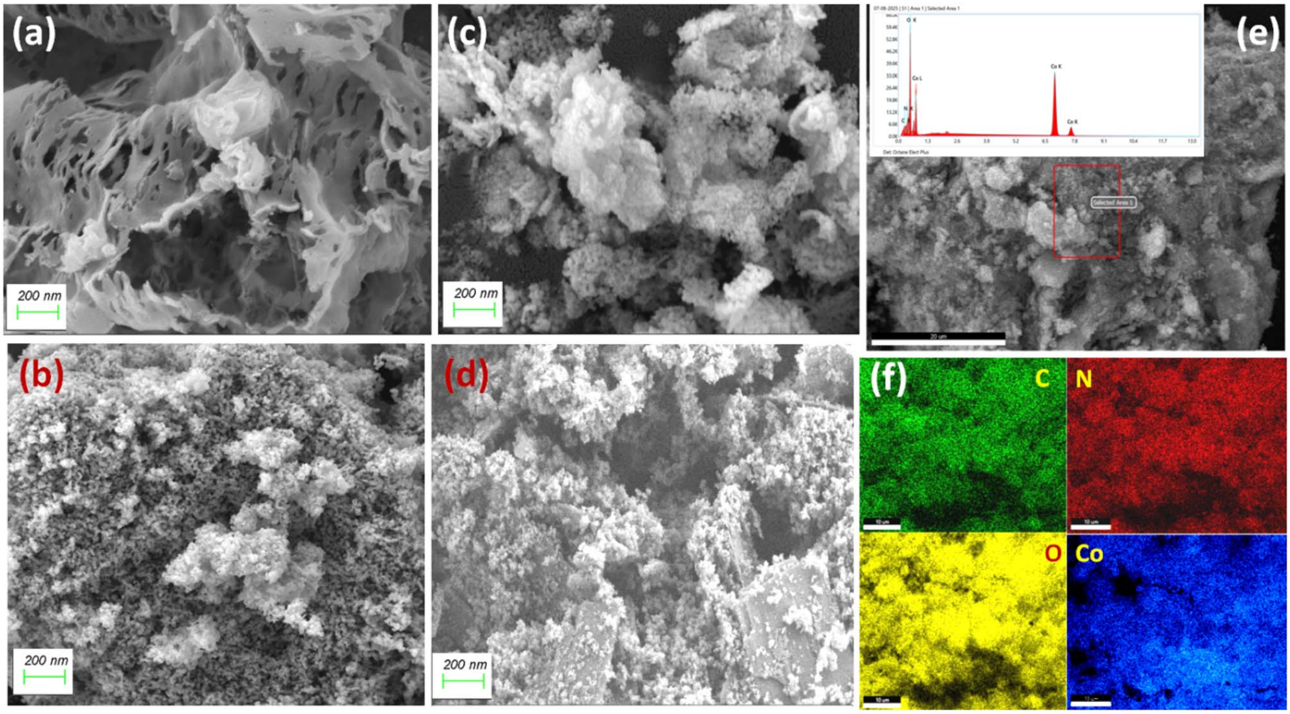

Fig. 1 SEM images of (a) D-CN, (b) CoO, and (c and d) the CoO/D-CN composite. (e) EDX spectrum and (f) elemental mapping of the CoO/D-CN composite.

Structural and surface analysis

To analyse the phase identification, crystallinity and phase purity of all the as-synthesized samples, they were analysed using XRD. The XRD patterns revealed the crystalline phases present in the CoO/D-CN heterojunction. Along with this, the sharpness of the peaks indicates high crystallinity, and the absence of additional peaks suggests good phase purity of both the pristine counterpart and the heterojunction. For instance, CoO exhibited characteristic peaks corresponding to its cubic structure, in pure form as well as in composite (Fig. 2(a)). While D-CN shows enhanced peaks as compared to g-C_3N_4, indicative of its exfoliated defect-containing layered structure (Fig. 2(b)). As can be observed in Fig. 2(a), the XRD pattern confirms the successful formation of a heterojunction between D-CN and CoO. CoO exhibited characteristic diffraction peaks corresponding to its cubic structure, which were observed in both the pure and composite forms. Meanwhile, D-CN displayed enhanced and broadened peaks compared with bulk g-C_3N_4, suggesting it has an exfoliated and defect-rich layered structure. As shown in Fig. 2(a), the composite displays all the characteristic diffraction peaks of cubic CoO for the (111), (200), (220), (311), and (222) planes, located at $2\theta \approx 36.5°$, 42.4°, 61.5°, 73.7°, and 77.5°, respectively, consistent with the standard JCPDS card No. 03-065-3103 (space group: $Fm\bar{3}m$, No. 225).[16–18] Additionally, a weak and broad feature around 18.7° (marked with *) corresponds to the in-plane and interlayer stacking of D-CN, confirming its defect-rich nature. The preservation of the CoO peaks in the composite pattern, albeit slightly shifted, indicates that its crystalline structure remains intact after coupling and confirms the formation of a heterojunction between the components. Notably, the composite exhibits higher diffraction intensities than pure CoO, which can be attributed to the introduction of D-CN as a highly dispersive and supportive matrix that inhibits nanoparticle agglomeration and promotes preferred orientation and improved crystallinity of CoO on the D-CN surface. Therefore, the enhanced peak intensity reflects strong interfacial coupling and high structural ordering of the CoO domains anchored on the D-CN substrate, confirming the successful formation of a well-integrated CoO/D-CN heterojunction.[19–25]

Additionally, Fig. 2(b) shows that the XRD patterns of pristine/pure g-C_3N_4 and the defect-containing g-C_3N_4 (D-CN) exhibit notable differences due to changes in the crystallinity, interlayer stacking, and in-plane structural ordering caused by the defects. The differences in the peaks of g-C_3N_4 and D-CN clearly reflect the introduction of structural disorder. In Fig. 2(c), the TEM image reveals the morphology of the D-CN, with visible defects in the structure of the layered structure. While in the TEM image of the CoO/D-CN composite (Fig. 2(d)), the CoO nanoparticles are uniformly dispersed over the layered D-CN sheets. The close interfacial contact suggests the efficient formation of a heterojunction, which is crucial for charge transfer during photocatalysis. In Fig. 2(e), the selected area electron diffraction (SAED) pattern displays distinct diffraction rings and spots, indicating the polycrystalline nature of the composite and the coexistence of the CoO and D-CN crystalline domains observed in the XRD.

Furthermore, Fig. 2(f) represents the textural properties of the different materials CoO, CoO/D-CN, and D-CN through

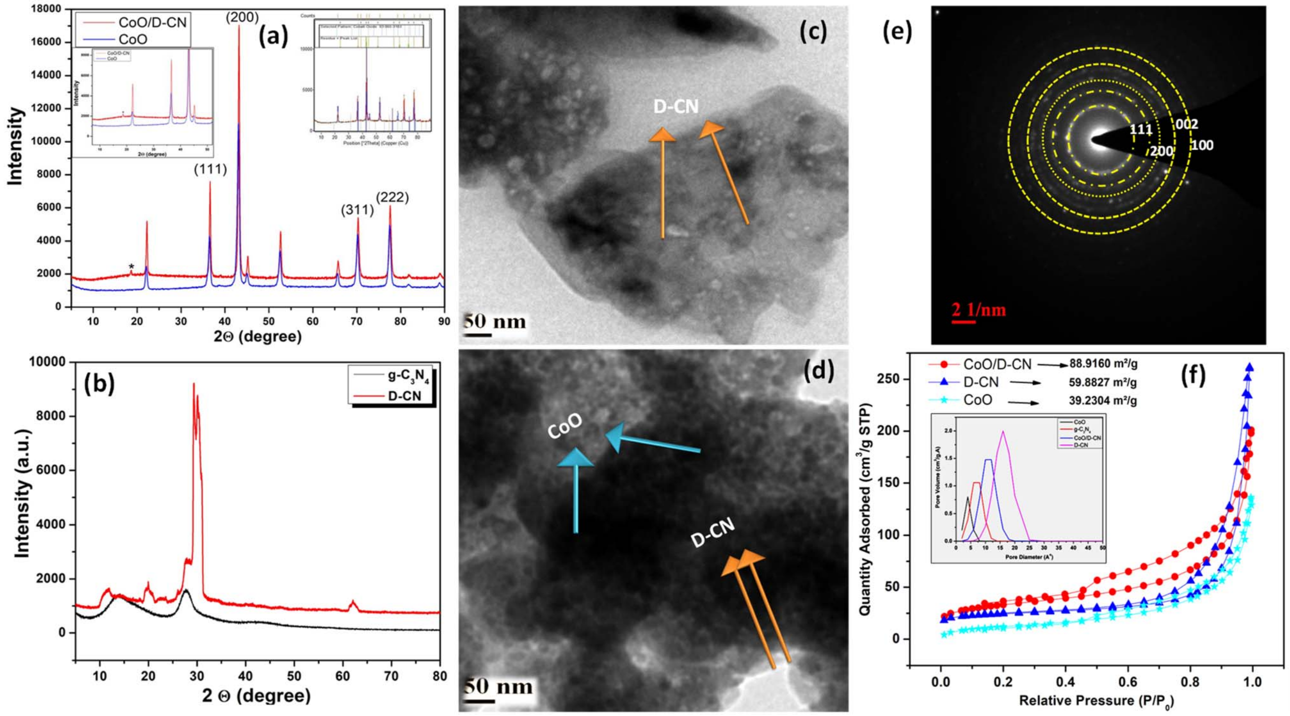

Fig. 2 XRD patterns of (a) CoO and the CoO/D-CN composite, and (b) neat g-C_3N_4 and the D-CN. TEM analysis of (c) D-CN and (d) the CoO/D-CN composite, (e) SAED pattern of the CoO/D-CN composite and (f) BET surface area and pore size analysis (inset) of the as-synthesised materials.

a BET surface area and pore size distribution (inset) analysis. In the figure, the BET surface area values are detailed as observed from the analysis. In our previously reported work, pristine g-C_3N_4 showed a relatively low surface area (~9.25 $m^2\ g^{-1}$),[14,15] indicating a limited number of exposed active sites due to their dense lamellar structures. In contrast, the composite CoO/D-CN and pure D-CN exhibited significantly higher surface areas (~88.9 and 59.8 $m^2\ g^{-1}$), respectively. The enhanced surface area of the D-CN sample as compared to the g-C_3N_4 implied that the structural modification effectively increased the porosity and created a more open framework, enhancing the adsorption and catalytic capabilities of the material. The high surface area value of the CoO/D-CN suggests that the integration of CoO nanoparticles with the defect-containing carbon nitride framework prevents particle agglomeration and introduces more accessible porosity and active sites in the structure. The inset figure displays the pore size distribution curves derived from the BJH method. CoO and g-C_3N_4 mainly exhibit narrow pore sizes centered around 4–8 Å. In contrast, CoO/D-CN and D-CN show broader and larger pore size distributions, around 12–18 Å, indicating the development of a porous structure created through defects. Overall, the data suggest that the synergistic structural modification (in CoO/D-CN and D-CN) significantly enhances both the surface area and pore structure, thereby improving the material performance in applications. This demonstrates that enhancing the surface area, active sites, and electronic properties of the synthesized material is important for photocatalysis and energy applications.

Optical properties

The optical properties of the pristine and the composites were evaluated, and the results are displayed in Fig. 3. The UV–vis diffuse reflectance spectra in Fig. 3(a) show that pure D-CN exhibits an absorption edge near 470 nm, while CoO extends into the visible region (~520 nm). In contrast to pristine g-C_3N_4, the D-CN absorption edge is red-shifted slightly, indicating band gap narrowing due to the defects. This demonstrates that defect engineering with enhanced visible-light absorption makes materials better suited for photocatalysis. The CoO/D-CN composite shows broader absorption, indicating enhanced visible-light harvesting due to synergistic band alignment. The new absorption peak appearing in the 600–800 nm region for the CoO/D-CN heterojunction (Fig. 3(a)) can be attributed to the synergistic interaction between the defect-engineered graphitic carbon nitride (D-CN) and CoO. Ascorbic acid-induced defects, such as nitrogen vacancies and surface functional groups, can introduce mid-gap states that facilitate interfacial charge transfer when coupled with CoO. Such charge-transfer transitions are well-documented in semiconductor–semiconductor heterojunctions, where electronic coupling extends light absorption into the visible–near-infrared region.[26,27] The defect-containing CN shows band gap narrowing due to the introduced mid-gap states, as evaluated using a Tauc plot. The composite (CoO/D-CN) has the lowest band gap, enhancing visible-light activity. This explains the improved photocatalytic behavior under solar illumination. In Fig. 3(b), the Tauc plots derived from the Kubelka–Munk function[28,29] estimate the band gaps of

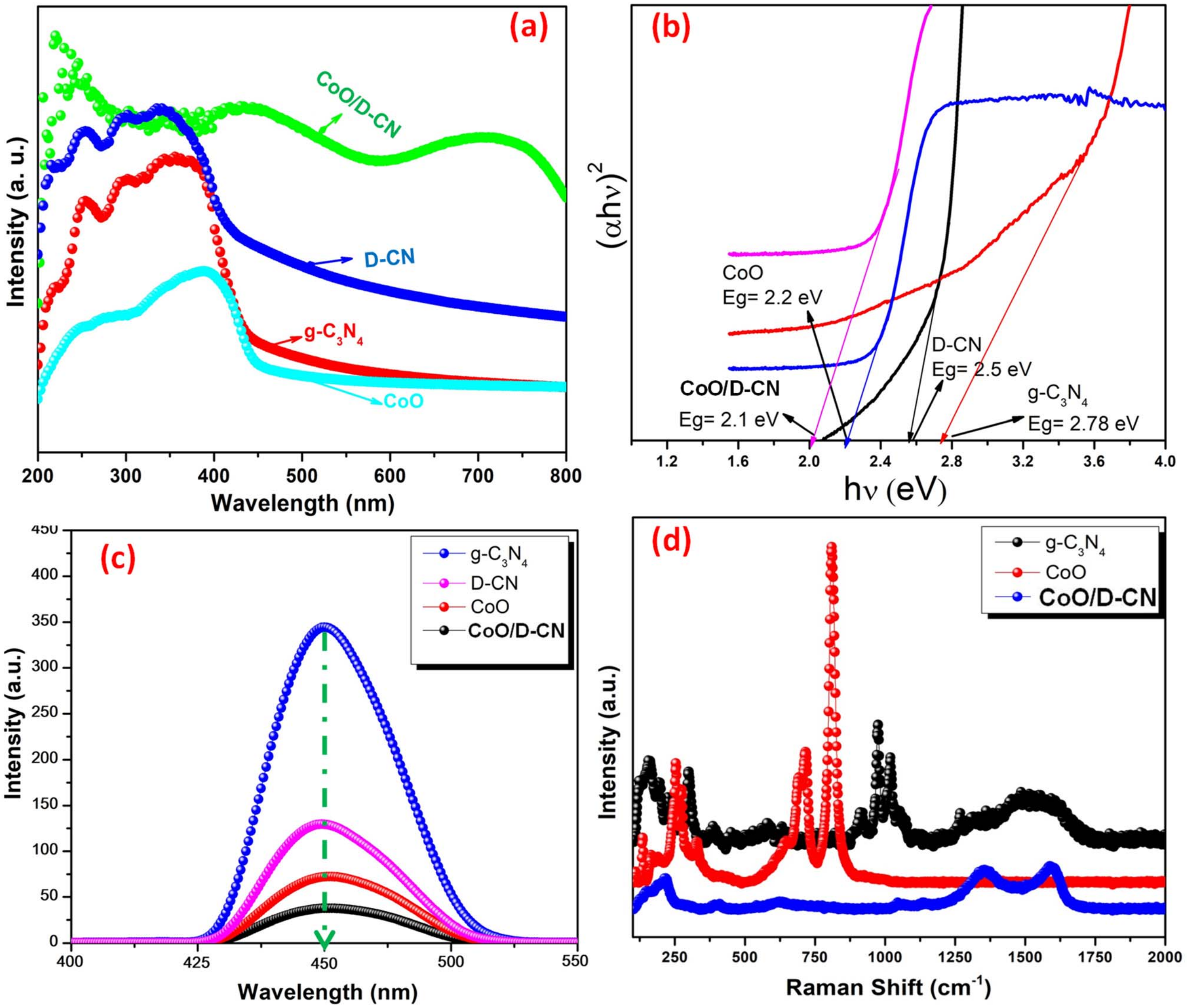

Fig. 3 (a) UV-vis absorbance spectra, (b) band gap analysis using Tauc plots, (c) photoluminescence spectra and (d) Raman spectra of pure g-C_3N_4, CoO, D-CN and the CoO/D-CN composite.

g-C_3N_4: ~2.78 eV, D-CN: ~2.5 eV (lower due to the defect states), CoO: ~2.2 eV (ref. 30) and D-CN/CoO: ~2.1 eV confirming successful heterojunction formation with improved light absorption properties.[31]

However, for the generation of H_2 or for BPA photocatalytic degradation, the conduction band (CB) and valence band (VB) edges of CoO and D-CN must provide sufficient overpotentials for redox reactions. According to the evaluated band gap values, the E_{CB} minima and E_{VB} maxima of CoO and D-CN were calculated using (eqn (1)) given below.[32]

$$E_{CB} = \chi - E_e - 0.5 \times E_g \quad (1)$$

Here, χ = the absolute electronegativity of the semiconductor (in eV), E_e = the energy of free electrons on the hydrogen scale ≈ 4.5 eV, and E_g = the band gap (in eV). Accordingly, the VB and CB band positions of each counterpart of the heterojunction were evaluated and are discussed further in the mechanism section.

To gain insight into the charge-separation aptitude of the designed heterojunction, photoluminescence (PL) analysis was conducted. Fig. 3(c) shows the PL spectra excited at 325 nm and indicates that g-C_3N_4 has a strong emission peak centered on 450 nm, suggesting high recombination of the charge carriers. Compared to other catalysts, the CoO/D-CN composite shows significantly quenched emission, confirming suppressed recombination and enhanced charge separation in the formed heterojunction. In Fig. 3(d), the Raman spectra further verify the structural integrity and interaction between the components. The characteristic peaks of D-CN and CoO are observed,[33–35] while the CoO/D-CN composite shows reduced intensity and peak shifts, indicating strong interfacial coupling and electronic interactions between the CoO and D-CN domains. Raman analysis confirms the structural modifications in the defect-containing CN and the strong chemical interactions in the composite, supporting the results of the other characterizations.

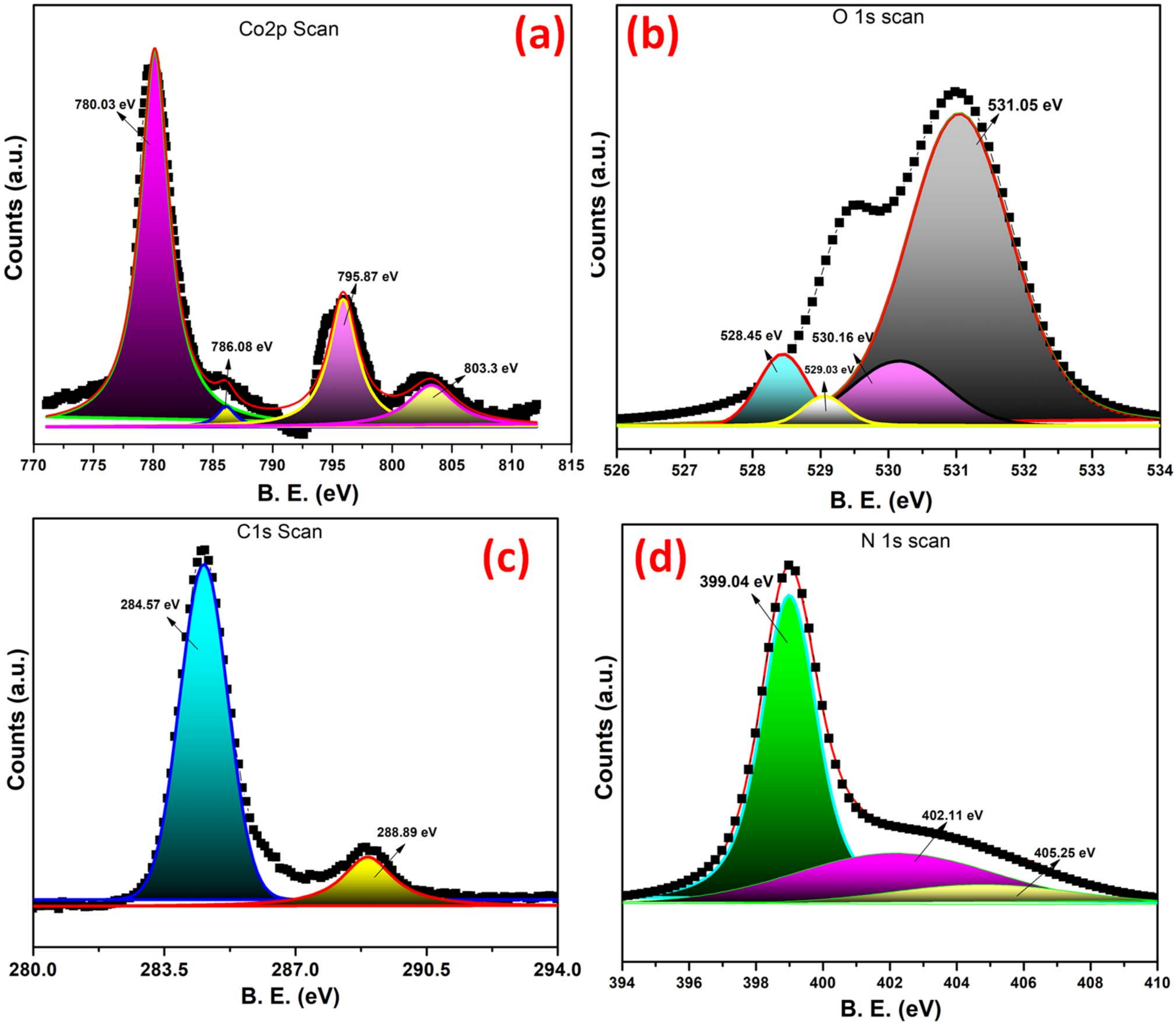

Fig. 4 XPS analysis of the CoO/D-CN composite showing the (a) Co 2p scan, (b) O 1s scan, (c) C 1s scan and (d) N 1s scan of the nanostructured composite.

XPS survey spectrum

The XPS data collectively confirm the successful formation of a CoO/D-CN heterojunction with intact chemical environments and strong interfacial interactions. To further examine the compositions and chemical states of the elements, XPS analysis was conducted. The surface features, especially the presence of Co^{2+} and nitrogen functionalities, play a vital role in enhancing the photocatalytic performance by facilitating charge transfer, reactive species formation, and interfacial bonding.[35–37]

Fig. 4(a) corresponds to the Co 2p spectrum and shows two main peaks at around 780.03 eV (Co $2p_{3/2}$) and 795.87 eV (Co $2p_{1/2}$), characteristic of the Co^{2+} in CoO. The accompanying satellite peaks at 786.08 eV and 803.3 eV confirm the presence of Co^{2+} species, indicating that cobalt exists predominantly as CoO with possible Co–N or Co–O–C coordination at the interface with D-CN. Fig. 4(b) displays the O 1s spectrum, which can be deconvoluted into three main components: (i) the peak at 528.46 eV corresponds to lattice oxygen (O^{2-}) in CoO; (ii) the one at 529.03–530.16 eV can be assigned to oxygen in the Co–O–C or Co–O–N linkages (defects or surface hydroxyl oxygen); and (iii) the broad peak at 531.05 eV related to adsorbed oxygen species or surface hydroxyl groups (–OH). These oxygen species suggest the coexistence of lattice and surface-bound oxygen, supporting catalytic activity. Fig. 4(c) shows the C 1s spectrum with a dominant peak at 284.57 eV, attributed to the sp^2-hybridized C–C/C=C bonds in graphitic carbon, and a secondary component at 288.89 eV corresponding to the N–C=N bonds within the defect-containing $g\text{-}C_3N_4$ framework.[34,35] The latter indicates partial oxidation or defect formation at carbon sites, thus enhancing interfacial reactivity. Finally, Fig. 4(d) depicts the N 1s spectrum, which can be resolved into peaks at 399.04 eV for the sp^2-hybridized C=N–C in the heptazine units, 402.11 eV for tertiary nitrogen N–(C)$_3$ or bridging N in N–(C)$_3$ configurations, and at 405.25 eV for oxidized N species, possibly N–O.[38,39] These features confirm the defect-containing nature of g-C_3N_4, where nitrogen vacancies and Co–N coordination likely form active sites for catalytic reactions. Moreover, The CoO/D-CN composite contains about 37 at% C, 28 at% N, 13 at% O, and 22 at% Co, giving ratios of Co/N ≈ 1 : 1.3 and Co/C ≈ 1 : 1.7. These ratios reflect the balanced integration of the CoO with the D-CN framework, confirming effective composite formation with well-distributed CoO active sites on the defect-containing carbon nitride surface.

Together, these XPS survey spectra reveal that the CoO/D-CN composite consists of Co^{2+} species anchored on nitrogen-rich defect-containing carbon nitride through Co–N and Co–O–C bonds, with abundant surface oxygen and nitrogen vacancies, features that enhance electronic coupling and catalytic functionality.

Photoactivity and recyclability test

Recent studies have shown that defect engineering and heterojunction design can significantly enhance photocatalytic performance. For instance, high-yield g-C_3N_4 nanostructures were synthesized *via* a supramolecular self-fission strategy for efficient hydrogen evolution,[40] while 2D/1D g-C_3N_4/a-WO_x amorphous heterojunctions enabled near infrared-driven hydrogen evolution.[41] Additionally, amorphous transition metal oxide-based 2D heterojunctions were shown to achieve superior photocatalytic hydrogen and oxygen evolution.[42] Building upon these precedents, the CoO/D-CN composite exhibits remarkable photocatalytic performance under visible-light irradiation, as demonstrated by the nearly complete degradation of hazardous BPA and its high hydrogen (H_2) evolution efficiency (Fig. 5). This enhanced activity arises from the formation of a heterojunction between the CoO and the defect-containing g-C_3N_4, which promotes efficient separation and transfer of photogenerated charge carriers. Upon visible-light irradiation, both CoO and D-CN absorb photons to generate electron–hole pairs.[43–47] Then, these distinct charge carriers in the heterojunction drive two important reactions: the holes oxidize BPA and form reactive oxygen species such as $\cdot OH$ and $\cdot O_2^-$ to help with the pollutant degradation pathway independently, while the electrons reduce water to produce hydrogen gas during the partial water splitting reaction.[9–13,33–42] Fig. 5(a) compares the BPA degradation efficiencies under light/dark conditions and different catalysts. Pure CoO and pristine g-C_3N_4 exhibit relatively low activity due to limited visible-light absorption and rapid charge recombination. The D-CN showed a notable increase in degradation efficiency, which can be attributed to nitrogen vacancies and structural defects acting as charge-separation centers. However, the CoO/D-CN composite achieves nearly complete BPA degradation (∼100%), evidencing a synergistic interaction between the CoO and defect-containing g-C_3N_4. This enhancement results from the formation of a heterojunction that facilitates efficient photogenerated charge carrier separation and transfer. The control experiments conducted in the dark with the CoO/D-CN heterojunction confirm that light is essential for catalytic activation, verifying the photocatalytic nature of the process. Fig. 5(b) displays the UV-vis absorption spectra of BPA at different irradiation times in the presence of the CoO/D-CN photocatalyst. The gradual decline and eventual disappearance of the main absorption peak near 276 nm, characteristic of BPA, indicate its progressive photodegradation. The systematic decrease in absorbance intensity with increasing illumination time (0–120 min) confirms the efficient breakdown of aromatic BPA molecules into less harmful and mineralized products. Fig. 5(c) shows the H_2 generation rates for various catalysts under visible-light irradiation. D-CN shows an improved H_2 evolution rate that is moderated through enhanced charge separation at the defect sites. In contrast, the CoO/D-CN composite displays a dramatic increase in H_2 evolution, reaching approximately 7600 ± 250 μmol h g^{-1}, highlighting the synergistic nature of the heterojunction interface between the CoO and D-CN. The inset photograph in Fig. 5(c) shows the actual photocatalytic setup with visible bubbling, visualizing the hydrogen generation. Fig. 5(d) evaluates the cyclic stability of the CoO/D-CN composite through four consecutive H_2 evolution runs. The nearly constant hydrogen production rates across the cycles indicate excellent durability and structural stability, with negligible loss in catalytic performance. Furthermore, Fig. 6 illustrates the recyclability of the CoO/D-CN catalyst during BPA degradation under visible-light irradiation. In Fig. 6 (a), the recyclability test over five consecutive runs shows consistent performance, indicating the stability and robustness of the CoO/D-CN catalyst. This stability may arise from the strong Co–N and Co–O–C linkages at the interface, which prevent photocorrosion and maintain charge-transfer efficiency. To examine the active species taking part in the BPA degradation, radical quenching experiments were carried out along with control experiments. Fig. 6 (b) explores the role of the reactive species by introducing specific quenchers for each radical. The significant reduction in BPA degradation efficiency upon the addition of isopropanol as the hydroxyl radical scavenger and benzoquinone as a superoxide radical scavenger confirms that both $\cdot OH$ and $\cdot O_2^-$ are the main active species responsible for the photocatalytic degradation of BPA.

Altogether, these photoactivity tests demonstrate that the CoO/D-CN composite functions as a robust bifunctional photocatalyst, which can effectively degrade organic pollutants like BPA and is also able to produce hydrogen under visible-light irradiation. The enhanced activity results from defect engineering in g-C_3N_4 and the formation of a CoO-based heterojunction, enabling efficient light harvesting, charge separation, and redox reaction kinetics. This is a well-designed example of how defect chemistry and semiconductor coupling can transform a simple material into a powerful solar-driven catalytic system.

Mechanism

The schematic illustration of the operating mechanism of the CoO/D-CN heterojunction in Fig. 7 shows the proposed photocatalytic reaction pathways of the CoO/D-CN

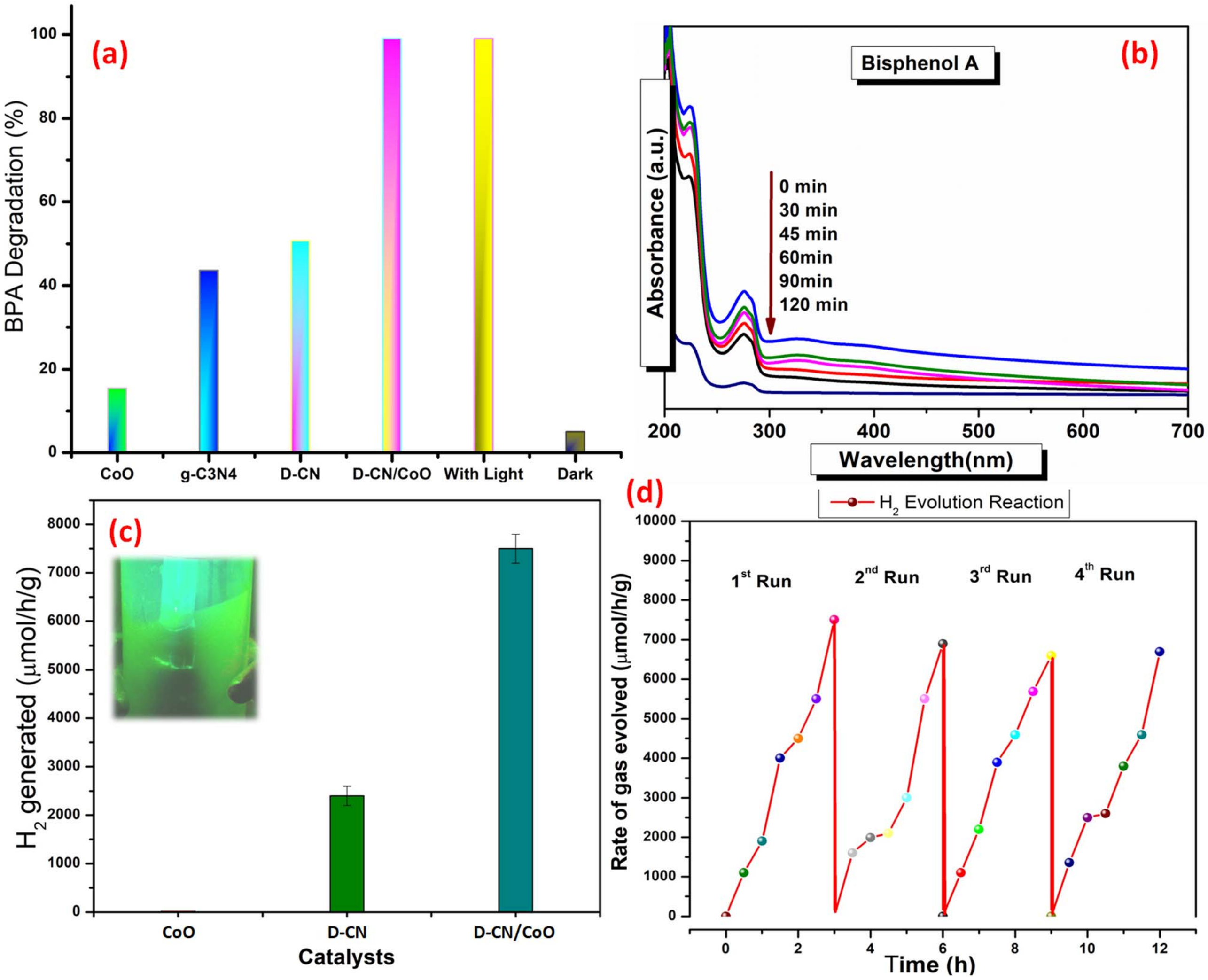

Fig. 5 (a) BPA degradation efficiency (%) of the as-synthesised catalysts, (b) UV-vis is analysis of BPA degradation over time (0–120 min) using the CoO/D-CN composite, (c) H_2 generation rates (μmol h^{-1} g^{-1}) for the different catalysts, and (d) the recyclability test of the CoO/D-CN catalyst for four consecutive runs of the H_2 generation reaction under visible-light illumination.

heterostructure under visible-light irradiation for BPA degradation and H_2 evolution. As described earlier, through the use of eqn (1), it is known that D-CN possesses a CB edge potential of −1.0 eV and a VB at +1.5 eV, while CoO has a CB at +0.85 eV and VB at +3.05 eV *versus* the normal hydrogen electrode (NHE). Initiated by visible-light excitation, both semiconductors absorb photons and generate (e^-–h^+) pairs. As per the band edge alignment, a conventional type-II transfer route could be expected for this composite. However, instead of a direct hole oxidation reaction, the radical trapping experiments show a sharp decline in photocatalytic activity in the presence of $\cdot$OH and $\cdot O_2^-$ radicals scavengers, indicating an alternative mechanism. Consequently, a direct Z-scheme mechanism can be expected in this case, as the positive conduction band of CoO and the low valence band of D-CN are unable to generate these radicals effectively due to their insufficient redox potentials. This unique Z-scheme charge transfer pathway enables the preservation of the strong oxidative holes in the VB of CoO (+3.05 eV) and the highly reductive electrons in the CB of D-CN (−1.0 eV). The Z-scheme mechanism was further validated, indicating that holes in the CoO VB generate $\cdot$OH radicals and the D-CN CB are responsible for O_2 reduction. These findings strongly support that the photogenerated charges follow a Z-scheme pathway instead of a type-II mechanism, maintaining high redox potentials on both sides of the heterojunction. Instead of undergoing direct recombination within the same semiconductor, the photogenerated electrons in the CB of CoO tend to recombine with the holes in the VB of the D-CN through an internal charge transfer pathway. The same charge transfer pathway is followed in the HER, and the D-CN electrons participate in proton reduction, which has a suitable hydrogen reduction potential. The highly negative CB electrons in the D-CN drive the reduction reactions, notably producing hydrogen.

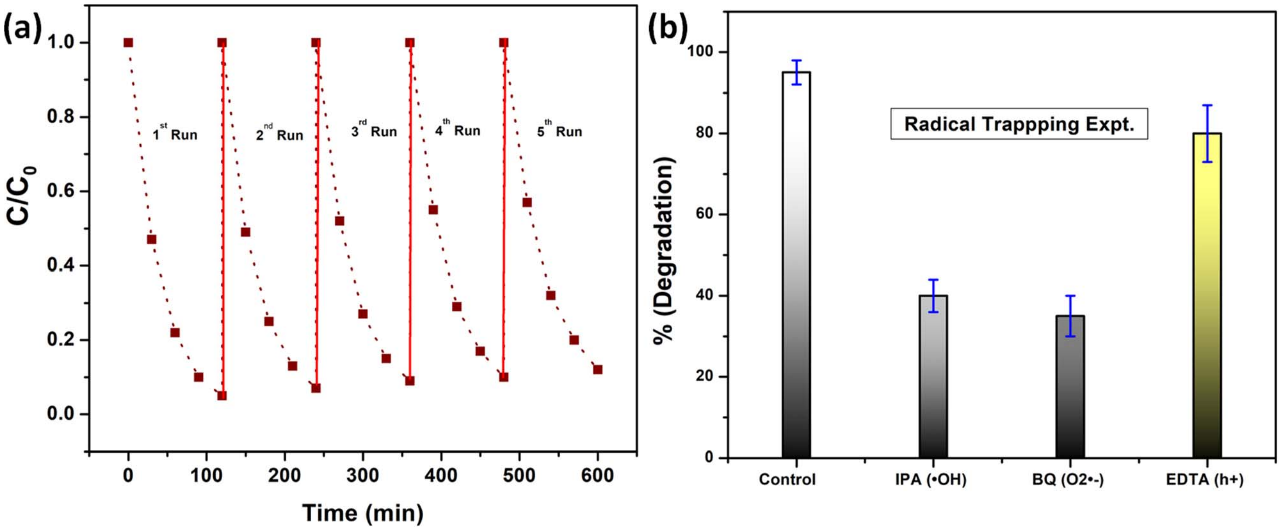

Fig. 6 (a) Recyclability test of the CoO/D-CN catalyst for five consecutive runs of BPA degradation under visible-light illumination. (b) Effect of the addition of quenchers on the photodegradation of BPA over the CoO/D-CN catalyst.

The novelty of this work lies in the rational construction of a direct Z-scheme heterostructure integrating CoO and defect-engineered carbon nitride, which not only overcomes the redox potential limitation of traditional type-II junctions but also leverages the defect-induced charge delocalization of the D-CN for enhanced electron mobility. The resulting CoO/D-CN composite exhibits dual-functional photocatalytic behavior with high efficiency for BPA degradation owing to the strongly oxidizing holes in the CoO. Additionally, this system can produce H_2 due to the highly reducing electrons in the D-CN. This synergy underscores a balanced photo-redox mechanism that few existing systems can achieve. The study thus provides a novel and practical pathway for designing multifunctional photocatalysts that harness visible light for both environmental remediation and renewable energy generation, positioning CoO/D-CN as a promising next-generation photocatalyst outperforming similar heterojunctions reported in prior works.

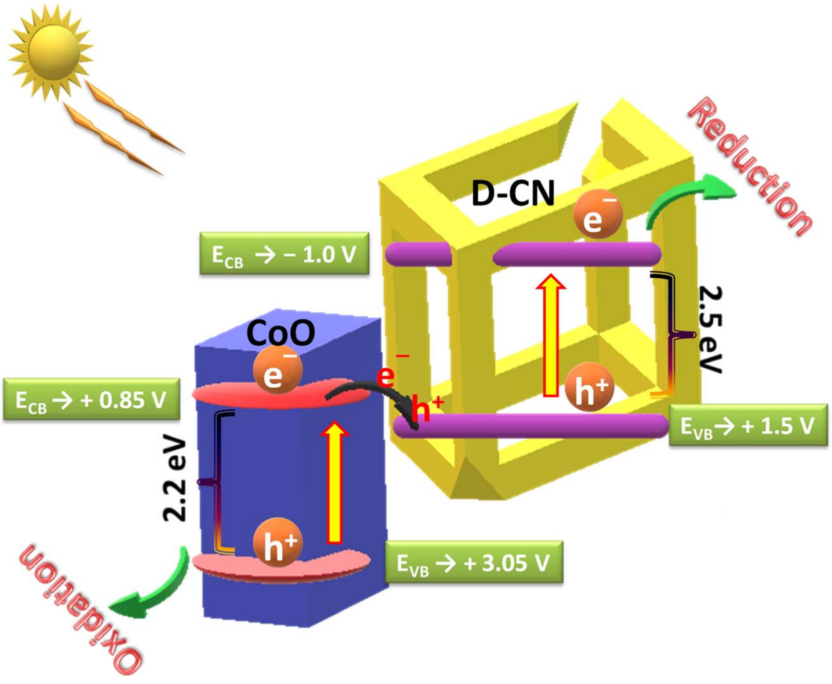

Fig. 7 Proposed mechanism explaining the photocatalytic efficacy of the CoO/D-CN composite under visible light irradiation for BPA degradation and H_2 generation.

Conclusion

Under visible light irradiation, the CoO/D-CN heterostructure exhibits remarkable dual-functional photocatalytic performance, achieving nearly total destruction of bisphenol A and markedly improved hydrogen evolution. The enhanced activity is ascribed to the formation of a composite, which results in effective charge separation and transfer, thus preserving robust redox potentials for both oxidation and reduction processes. In addition to promising photocatalytic performance, the composite shows outstanding stability and recyclability across a number of cycles. These findings demonstrate that this system is a potentially viable and sustainable photocatalyst for concurrent clean energy production and environmental remediation.

Author contributions

Sudhansu Sekhar Behera and Alaka Samal: made substantial contributions to the conception and design of the study and performed data analysis and interpretation. Nigamananda Das: performed data acquisition, as well as providing administrative, technical, and material support. Sudhansu Sekhar Behera, Alaka Samal, Arundhati Barik, and Nigamananda Das: writing and review of the original draft. All authors have read and agreed to the published version of the manuscript.

Conflicts of interest

The authors declare no conflicts of interest.

Data availability

All data generated or analyzed during this study are included in this article. No external repositories were used. The data that support the findings of this study will be available on request from the corresponding authors.

Acknowledgements

The authors acknowledge the Centre of Excellence in Advanced Materials and Applications (CAMA), Department of Chemistry, Utkal University, Odisha for providing the necessary facilities and support.

References

1 I. Arora, H. Chawla, A. Chandra, S. Sagadevan and S. Garg, *Inorg. Chem. Commun.*, 2022, **143**, 109700, DOI: 10.1016/j.inoche.2022.109700.
2 S. J. A. Moniz, S. A. Shevlin, D. J. Martin, Z.-X. Guo and J. Tang, *Energy Environ. Sci.*, 2015, **8**, 731–759, DOI: 10.1039/C4EE03271C.
3 Z. Zhang, L. Bai, Z. Li, Y. Qu and L. Jing, *J. Mater. Chem. A*, 2019, **7**, 10879–10897, DOI: 10.1039/C9TA02373A.
4 S. Weon, F. He and W. Choi, *Environ. Sci.: Nano*, 2019, **6**, 3185–3214, DOI: 10.1039/C9EN00891H.
5 J. O. Ighalo, S. B. Kurniawan, B. Khongthaw, J. Buhari, P. K. Chauhan, J. Georgin and D. S. Pfingsten Franco, *RSC Adv.*, 2024, **14**, 35128–35162, DOI: 10.1039/D4RA05628K.
6 P. Wang, X. Zhou, Y. Zhang, L. Wang, K. Zhi and Y. Jiang, *RSC Adv.*, 2016, **6**, 102348–102358, DOI: 10.1039/C6RA23542E.
7 M. Verelst, T. O. Ely, C. Amiens, E. Snoeck, P. Lecante, A. Mosset, M. Respaud, J. M. Broto and B. Chaudret, *Chem. Mater.*, 1999, **11**, 2702–2708, DOI: 10.1021/cm991003h.
8 M. Ghosh, E. V. Sampathkumaran and C. N. R. Rao, *Chem. Mater.*, 2005, **17**, 2348–2352, DOI: 10.1021/cm0478475.
9 A. B. Naveed, A. Javaid, A. Zia, M. T. Ishaq, M. Amin, Z. U. R. Farooqi and A. Mahmood, *ACS Omega*, 2023, **8**, 2173–2182, DOI: 10.1021/acsomega.2c04841.
10 B. Liu, C. Bie, Y. Zhang, L. Wang, Y. Li and J. Yu, *Langmuir*, 2021, **37**, 14114–14124, DOI: 10.1021/acs.langmuir.1c02360.
11 F. Guo, W. Shi, H. Wang, M. Han, H. Li, H. Huang, Y. Liu and Z. Kang, *Catal. Sci. Technol.*, 2017, **7**, 3325–3331, DOI: 10.1039/C7CY00960G.
12 Y. Han, Z. Wang, X. Yang, Z. Li and Y. Li, *Catalysts*, 2025, **15**(4), 315, DOI: 10.3390/catal15040315.
13 Z. Wang and F. Labat, *J. Mater. Chem. A*, 2025, **13**, 3115–3131, DOI: 10.1039/D4TA07907H.
14 C. Mohanty, A. Samal, J. Kumar, A. K. Behera, R. Das and N. Das, *Int. J. Hydrogen Energy*, 2025, **120**, 628–641, DOI: 10.1016/j.ijhydene.2025.03.193.
15 C. Mohanty, A. Samal and N. Das, *Int. J. Hydrogen Energy*, 2024, **61**, 84–93, DOI: 10.1016/j.ijhydene.2024.02.266.
16 Q. Qi, Y. Chen, L. Wang, D. Zeng and D.-L. Peng, *Nanotechnology*, 2016, **27**, 455602, DOI: 10.1088/0957-4484/27/45/455602.
17 Y. Sun, J. Zhang, S. Liu, X. Sun and N. Huang, *Nanotechnology*, 2021, **32**, 195707, DOI: 10.1088/1361-6528/abe264.
18 (*a*) M. A. Ehsan, A. S. Hakeem and A. Rehman, *Electrocatalysis*, 2020, **11**, 282–291, DOI: 10.1007/s12678-020-00585-z; (*b*) L. Liao, Q. Zhang, Z. Su, Z. Zhao, Y. Wang, Y. Li, *et al.*, *Nat. Nanotechnol.*, 2014, **9**, 69–73.
19 Z. Lin, J. Zhang, K. Zhang, W. Zhong, Y. Yang, J. Sun and J. Liu, *J. Mol. Catal. A: Chem.*, 2019, **486**, 110–118, DOI: 10.1016/S0021-9517(19)30133-2.
20 Z. Y. Mao, J. J. Chen, X. Q. Zhang, Y. H. Sun, L. F. Zhang, R. J. Wang and X. J. Zhang, *ACS Appl. Mater. Interfaces*, 2017, **9**, 12525–12534, DOI: 10.1021/acsami.7b00370.
21 Y. Zhou, J. Shi, H. Li, Y. Ding, F. Han and X. Liu, *Ceram. Int.*, 2018, **44**, 18181–18188, DOI: 10.1016/S0272-8842(18)31569-4.
22 L. Chang, Y. Yang, M. Fang and X. Zhang, *Electrochim. Acta*, 2017, **255**, 366–374, DOI: 10.1016/S0925-8388(17)32487-8.
23 L. Zhang, Z. Wang, H. Wang, K. Yang, L. Wang, X. Li, Y. Zhang and H. Dong, *J. Alloys Compd.*, 2016, **656**, 278–283, DOI: 10.1016/j.jallcom.2015.09.208.
24 Y. Guan, X. Zhang, Y. Li, G. Wang, J. Chen, H. Zhang and Y. Yu, *Electrochim. Acta*, 2020, **345**, 136199, DOI: 10.1016/S0013-4686(20)30485-0.
25 P. Vijayakumar, N. Sethupathi, S. Manikandan, P. Mahalingam, P. Maadeswaran and K. A. Rameshkumar,

Ionics, 2024, **30**, 7489–7501, DOI: 10.1007/s11581-024-05815-8.

26 Y. X. Zhu, T. Wan, X. Wen, D. Chu and Y. Jiang, *Appl. Catal., B*, 2019, **244**, 814–822, DOI: 10.1016/j.apcatb.2018.12.015.

27 X. Xu, S. Dong, J. Lv, G. Huang, Q. Chen and J. Bi, *Appl. Surf. Sci.*, 2025, **689**, 162489, DOI: 10.1016/j.apsusc.2025.162489.

28 C. Li, Z. Sun, Y. Xue, G. Yao and S. Zheng, *Adv. Powder Technol.*, 2016, **27**(2), 330–337, DOI: 10.1016/j.apt.2016.01.003.

29 B. Li, F. Zhang, Y. Liu, H. Yin, J. Zou and A. Ou-yang, *RSC Adv.*, 2022, **12**, 28152–28170, DOI: 10.1039/D2RA04635K.

30 N. Alidoust and E. A. Carter, *J. Appl. Phys.*, 2016, **119**, 025102, DOI: 10.1063/1.4939286.

31 X. Hong, X. Luo, X. Xu, P. Ji, S. Yue and R. Li, *Sep. Purif. Technol.*, 2023, **327**, 124948, DOI: 10.1016/j.seppur.2023.124948.

32 P. George and P. Chowdhury, *Analyst*, 2019, **144**, 3005–3012, DOI: 10.1039/C8AN02257G.

33 P. Vijayakumar, N. Sethupathi, S. Manikandan, P. Mahalingam, P. Maadeswaran and K. A. Rameshkumar, *Ionics*, 2024, **30**, 7489–7501, DOI: 10.1007/s11581-024-05815-8.

34 A. Samal, S. Swain, B. Satpati, D. P. Das and B. K. Mishra, *ChemSusChem*, 2016, **9**, 3150–3160, DOI: 10.1002/cssc.201601214.

35 L. Zhou, M. Xu, W. Zhang and X. Yao, *Nanoscale*, 2025, **17**, 15879–15888, DOI: 10.1039/D5NR01499A.

36 F. Xie, J.-F. Guo, H.-T. Wang and N. Chang, *Colloids Surf., A*, 2022, **636**, 128157, DOI: 10.1016/j.colsurfa.2021.128157.

37 X. Qian, W. Li, X. Wang, H. Guan, Q. Bao, B. Zhao, B. Wulan, S. Liu, D. Zhu, X. Feng and J. Sun, *Adv. Funct. Mater.*, 2025, **35**, 2416946, DOI: 10.1002/adfm.202416946.

38 S. Chen, D. Huang, M. Cheng, L. Lei, Y. Chen, C. Zhou, R. Deng and B. Li, *J. Mater. Chem. A*, 2021, **9**, 196–233, DOI: 10.1039/D0TA08165E.

39 K. Krumova and G. Cosa, *Methods Appl. Fluoresc.*, 2016, **4**, 022003, DOI: 10.1088/2050-6120/4/2/022003.

40 B. X. Zhou, C. Zhang, Y. Li, S. Ding, L. Meng, H. Jing, H. Ye, Y. Liu, C. Tian, A. Zhou, G.-F. Huang and W.-Q. Huang, *J. Colloid Interface Sci.*, 2025, **695**, 137787, DOI: 10.1016/j.jcis.2025.137787.

41 B. X. Zhou, H. L. Ye, Y. Y. Li, C. Zhang, S. S. Ding, L. X. Meng, H. J. Jing, Y. B. Liu, C. C. Tian, A. G. Zhou, G.-F. Huang and W.-Q. Huang, *Sep. Purif. Technol.*, 2025, **372**, 133455, DOI: 10.1016/j.seppur.2025.133455.

42 B.-X. Zhou, S.-S. Ding, K.-X. Yang, J. Zhang, G.-F. Huang, A. Pan, W. Hu, K. Li and W.-Q. Huang, *Adv. Funct. Mater.*, 2021, **31**, 2009230, DOI: 10.1002/adfm.202009230.

43 B. X. Zhou, C. Zhang, Y. Y. Li, S. S. Ding, L. X. Meng, H. J. Jing, H. L. Ye, Y. B. Liu, C. C. Tian, A. G. Zhou, G.-F. Huang and W.-Q. Huang, *J. Colloid Interface Sci.*, 2025, **695**, 137787, DOI: 10.1016/j.jcis.2025.137787.

44 X.-R. Wang, K.-X. Yang, S.-S. Ding, Y.-Y. Li, B.-X. Zhou, G.-F. Huang, A. Pan, W. Hu, K. Li and W.-Q. Huang, *Phys. Status Solidi RRL*, 2021, **15**, 2100254, DOI: 10.1002/pssr.202100254.

45 H. R. Ahmed, K. H. Hama Aziz, N. N. M. Agha, F. S. Mustafa and S. J. Hinder, *RSC Adv.*, 2023, **13**, 26252–26266, DOI: 10.1039/D3RA04566H.

46 K. Michalec, B. Mozgawa, A. Kusior, P. Pietrzyk, Z. Sojka and M. Radecka, *J. Phys. Chem. C*, 2024, **128**(12), 5011–5029, DOI: 10.1021/acs.jpcc.3c08165.

47 B. Gao, S. Iftekhar, V. Srivastava, B. Doshi and M. Sillanpää, *Catal. Sci. Technol.*, 2018, **8**, 2186–2194, DOI: 10.1039/C8CY00303C.